

**A CLINICAL PROTOCOL TO VALIDATE A BREAST
CONSERVATIVE THERAPY OUTCOME MODEL**

A Thesis

Presented to

the Faculty of the Department of Computer Science

University of Houston

In Partial Fulfillment

of the Requirements for the Degree

Master of Science

By

Nicole Lepoutre

August 2013

**A CLINICAL PROTOCOL TO VALIDATE A BREAST
CONSERVATIVE THERAPY OUTCOME MODEL**

Nicole Lepoutre

APPROVED:

Dr. Marc Garbey, Chairman
Dept. of Computer Science
University of Houston

Dr. Barbara Lee Bass
Dept. of Surgery
The Methodist Hospital Research Institute

Dr. Victoria Hilford
Dept. of Computer Science
University of Houston

Dean, College of Natural Sciences and Mathematics

Acknowledgements

My special thanks go out to my advisor Dr. Marc Garbey from University of Houston, who chose me to work in his lab and gave me much support and advice. I would like to thank both Dr. Garbey and Dr. Barbara Bass, the head of the Department of Surgery from Houston Methodist for giving me a very interesting project topic.

I would like to thank my co-advisor Pr. Christophe Collet from the University of Strasbourg for the follow-up of my international mobility and who offered me rich and helpful recommendations.

I would also particularly like to thank Marlene Gilles for helping me move to Houston and for reviewing her work with me. She helped me understand what the aim of my work is, even though she was under no obligation to.

My appreciation goes out to the University of Houston and the Houston Methodist employees who helped me with all the administrative paperwork to come study at UH but and to work in the hospital. I would like to convey thanks especially to Linda Moore, Joan Zampieri, and Debra Morris for their kindness and help during this year.

My sincere thanks go out to all those who worked hard to set up the Atlantis Program, including but not limited to Pr. Christophe Collet, Pr. Bernard Bayle, and Pr. Marc Garbey. I also greatly appreciate Pr. Giuseppe Baselli's organization of the summer school in Milan.

I would like to express my gratitude to my committee member Dr. Victoria Hilford for her cooperation and outstanding classes.

I also would like to thank the European Union, the dual degree Atlantis CRISP program, and the Alsace Region who provided me financial support.

Special thanks to all the members of the team for answering all my questions, helping me and making this year a wonderful experience.

Finally, and most importantly, a huge thank you to my parents and sisters who supported me during my studies and encouraged me to reach my dreams.

**A CLINICAL PROTOCOL TO VALIDATE A BREAST
CONSERVATIVE THERAPY OUTCOME MODEL**

An Abstract of a Thesis

Presented to

the Faculty of the Department of Computer Science

University of Houston

In Partial Fulfillment

of the Requirements for the Degree

Master of Science

By

Nicole Lepoutre

August 2013

Abstract

Breast cancer is the most common cancer among women around the world. Regarding the different treatments modalities for breast cancer, one is Breast Conservative Therapy (BCT) where the complete tumor and a margin of healthy tissues are surgically removed and the remaining breast tissue receives radiotherapy. From a patient point of view, preserving the shape of her breast is essential for her quality of life and hence, BCT may be a good treatment option. Although the outcome of this treatment usually provides good clinical results, some cosmetic defects like asymmetry may emerge. The goal of our team is to offer surgeons a tool that predicts the shape of the breast after BCT. Therefore, a multiscale model has been implemented by members of our team and is being validated and fine-tuned. A clinical study has been designed. The objective of this Master's thesis is to determine whether the predicted shape of the breast is realistic or not by:

- acquiring numerical data during the patients' follow-up,
- providing a confident 3D-reconstruction of the breast at certain point in time,
- understanding the main steps during the healing process.

Contents

1	Introduction	1
1.1	Breast cancer	1
1.1.1	Anatomy of the breast	2
1.1.2	Types and stages	3
1.1.3	Diagnosis	4
1.1.4	Treatments	5
1.2	Computational framework	6
1.3	Objective of our work	8
2	State-of-the-art	10
2.1	Active systems	11
2.1.1	Structured light	11
2.1.2	Time-of-flight	13
2.2	Multiview stereoscopic reconstruction	15
3	Clinical Study	16
3.1	Protocol of the study	16
3.2	Acquired data	18
3.2.1	MRI	18
3.2.2	Ultrasound images	19

3.2.3	Thermal imaging	19
3.2.4	Surface imaging	20
3.2.5	Quality of life	21
4	3D Reconstruction	22
4.1	Background	23
4.1.1	Coordinate systems	23
4.1.2	Calibration	24
4.1.3	Point matching	26
4.1.4	Computation of the 3D-coordinates	28
4.2	Improvements on the stereoscopic reconstruction	29
4.2.1	Preprocessing	30
4.2.2	3D coordinates computation	42
4.2.3	Postprocessing	43
5	Results and discussion	45
5.1	3D-reconstruction	45
5.2	Comparison with another system	46
5.2.1	Kinect	47
5.2.2	Discussion	48
5.3	Validation	49
5.3.1	Comparison of cross-sections in the sagittal plane	49
5.3.2	Accuracy of the stereoscopic system	50
5.4	Analysis of the first patient data	51
6	Conclusion	57
	Bibliography	59

List of Figures

1.1	Anatomy of the woman breast from [18]	2
1.2	Steps to model the shape of the breast after BCT, from [25]	7
2.1	Kinect sensor developed by Microsoft from [17]	12
3.1	Clinical study time-line showing the follow-up and the acquired data	17
3.2	MRI image of the breasts in the transverse plane	18
3.3	3D surface reconstruction of the MRI data set	18
3.4	Example of US images (a) in transverse plane. (b) in coronal plane.	19
3.5	Thermal imaging. (a) E60 FLIR camera from [10]. (b) Picture of a breast taken with our E60 FLIR camera.	20
3.6	Our stereoscopic system made up of two cameras, a videoprojector and a laptop	21
4.1	Pattern illustrating the different notions in epipolar geometry from [34]	27
4.2	Geometry to compute the 3D-coordinates thanks to the triangulation method	28
4.3	Difference of Gaussians filter implemented to detect the projected lines	31
4.4	Image presenting high variations of light intensity, the cyan circle gives an example of a bright part while the dark blue one reveals a dark part	32
4.5	Histogram marking the thresholds in order to cut the image out different parts	33

4.6	Cross-section of a common acquired image proving the intensity of the light is not uniform	36
4.7	Result of the Fourier Transform on the image where the black circle exhibits the main spike of the sinc	38
4.8	Blurred image accessed after eliminating unwanted frequencies in the Fourier domain	39
4.9	Results of the images subtraction that afford a clear image to process	40
4.10	Cross-section after subtraction at the level of the nipples proving a threshold is sufficient to segment properly the lines	41
4.11	Achieved image after applying the Gabor filter	42
4.12	Image rectification (a) Unrectified stereoscopic pair (b) Rectified stereoscopic pair pointing out two matched point have the same y-coordinate.	43
5.1	Results for the mannequin 3D-reconstruction (a) Overall view (b) View showing the artificial defect on the breast	45
5.2	Results for the patient's right breast 3D-reconstruction (a) in the coronal plane (b) in the sagittal plane	46
5.3	Reconstruction with Microsoft Kinect processed by RecFusion	48
5.4	Comparison of the cross-section between the real mannequin (blue curve) and the Kinect reconstruction (green curve)	49
5.5	Validation structure to gauge the accuracy of our stereoscopic system	50
5.6	Comparison between the theoretical time-line of the protocol and the follow-up of our first patient	52
5.7	Difference of height between the two breasts during the healing process for our first patient	53
5.8	Evolution of the difference of volume between the two breasts during the healing process for our first patient	54
5.9	Evolution of the temperature for both breasts during the healing process for our first patient	55

List of Tables

1.1	Different types of breast cancer	3
1.2	Different stages of breast cancer	4
1.3	Main treatments against breast cancer that a doctor can stipulate according to the stage and the type	5
4.1	Comparison between Cartesian and homogeneous coordinates for transformation matrices	24

Chapter 1

Introduction

1.1 Breast cancer

Breast cancer is a disease in which a tumor appears in a breast and grows uncontrollably. Breast cancer is the most common cancer among women since about 1 in 8 women will be diagnosed with it in their lifetime. According to the World Health Organization [32] and a breast cancer organization [3], in 2011, 230, 480 women were newly diagnosed with having invasive breast cancer in the United States and around 40, 000 people died from this illness the same year.

1.1.1 Anatomy of the breast

The breast consists of glandular tissue and adipose tissue (fat cells). Throughout the breast, there is a network of ligaments, fibers, nerves, blood vessels and lymph nodes and vessels. The breast overlies the pectoral muscles. The glandular tissue is divided into 12 to 20 sections called lobes. Each lobe consists of many smaller lobules that contain the glands that produce milk in nursing women. Ducts connect lobes and lobules to the nipple to deliver milk. Lymph nodes contain immune system related tissues and infection fighting cells. Figure 1.1 exposes the anatomy of the woman breast.

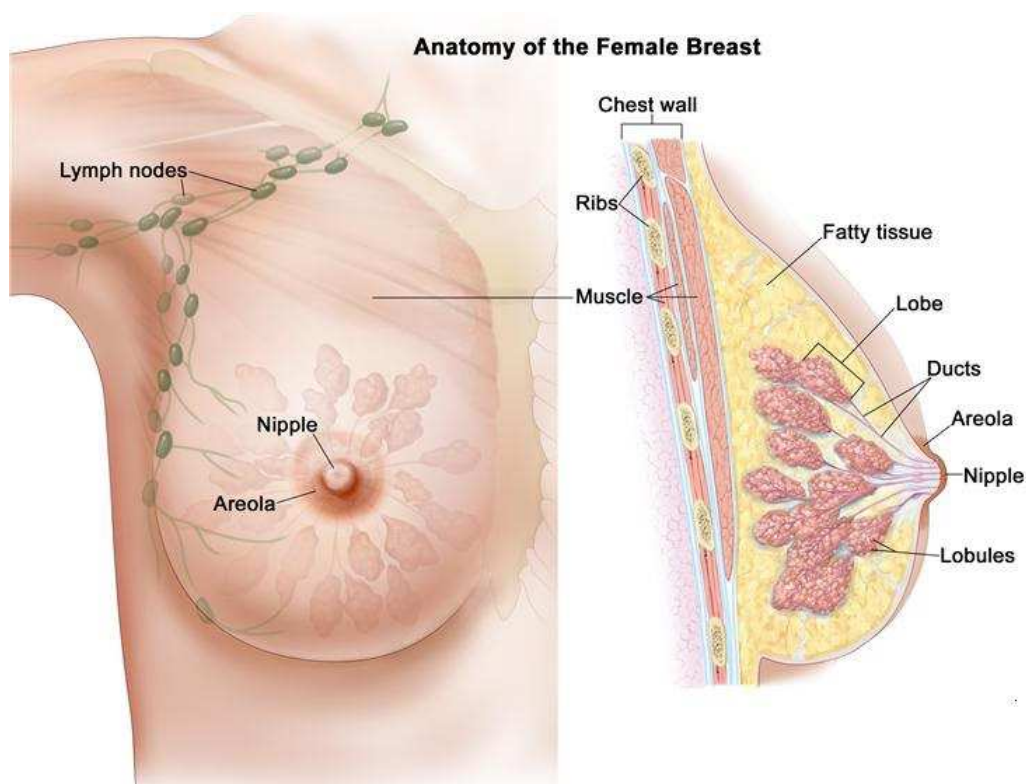


Figure 1.1: Anatomy of the woman breast from [18]

1.1.2 Types and stages

A human organ is normally composed of healthy cells. However, DNA cells can be damaged which causes abnormal reproduction of mutated cells. This growth of abnormal cells can form a benign or malignant tumor. Malignant tumors are better-known as cancer. The different types of breast cancer are classified mainly according to the origin of the tumor and how it has spread as table 1.1 shows [3].

Type	Origin	Spreading
Lobular Carcinom in Situ	Lobules	Spreading to milk ducts
Ductal Carcinoma in Situ	Milk ducts	-
Invasive Ductal Carcinoma	Milk ducts	Spreading beyond the ducts into other parts of the breast tissue
Inflammatory Breast Cancer	Skin and lymph vessels of the breast	Spreading to vessels of the breast
Metastatic Breast Cancer	Breast	Speading to other parts of the body

Table 1.1: Different types of breast cancer

Breast cancer is also divided into different stages. Each stage depends on the size of the tumor and how it has spread. The table 1.2 itemizes them.

Stage	Tumor size	Spreading
0	-	Abnormal cells in the breast duct
I-A	< 2cm	No spreading to the lymph nodes
I-B	< 2cm	Some cancer cells in lymph nodes
II-A	< 2cm	Spreading to axillary lymph nodes
	2cm < size < 5cm	No spreading to underarm lymph nodes
II-B	2cm < size < 5cm	Spreading to axillary lymph nodes
	> 5cm	No spreading to axillary lymph nodes
III-A	< 5cm	Spreading to axillary lymph nodes May have spread to lymph nodes behind the sternum
	> 5cm	May have spread to lymph nodes behind the sternum
III-B	Any size	Spreading to axillary lymph nodes May have spread to lymph nodes behind the breastbone
III-C	Any size	Spreading to lymph nodes behind the sternum and under the arm May have spread to lymph nodes above or below the clavicle
IV	Any size	Spreading to other parts of the body (e.g. lungs, liver, bones, etc)

Table 1.2: Different stages of breast cancer

1.1.3 Diagnosis

The diagnosis of breast cancer is in part done with imaging. Most of patients undergo a mammogram in which doctors can detect the early formation of tumors. In some very particular cases, patients also have to undergo a MRI scan. Then, a biopsy is performed. During a biopsy, doctors remove a small part of the tumor which is analyzed in order to determine if the tumor is benign or malignant. At the end of this step, patients and doctors may know the stage and the type of breast cancer.

1.1.4 Treatments

The treatment is planned by considering the type of breast cancer and the stage of the disease. The earlier the cancer is diagnosed, the more treatment options a doctor can recommend. The main approaches are surgery and medical therapy (chemotherapy, radiotherapy, etc). Table 1.3 shows different choices a doctor and a patient can have [1].

Approach	Treatment	Main idea
Surgery	Mastectomy	Remove the whole breast
	Lumpectomy	Remove a part of the breast
Therapy	Radiotherapy	Kill cancer cells with X-rays
	Chemotherapy	Kill cancer cells with drugs
	Hormone therapy	Stop or slow the growth of the tumor
	Targeted therapy	Stop or slow the spread out with drugs

Table 1.3: Main treatments against breast cancer that a doctor can stipulate according to the stage and the type

Surgery (mastectomy or lumpectomy) is almost always performed in early stages of breast cancer. Chemotherapy is considered in more critical stages. However, typically, patients receive more than one treatment. In our study, we concentrate on the combination of lumpectomy and radiotherapy which is called Breast Conservative Therapy (BCT).

1.2 Computational framework

After BCT, there is usually a change to the shape and contour of the breast. There has not been significant research in finding ways to improve BCT outcomes from a cosmetic standpoint. To our knowledge, our team is the first to develop a model to predict the shape of the breast after lumpectomy and radiotherapy. Members of our team have been working on the theoretical outcome of the breast after BCT. According to the work of D. Thanoon et al. [25], the different factors which seem influence the outcome are:

- mechanical parameters of the breast tissues,
- distribution of tissues in the breast,
- advancement of the healing process,
- change of the mechanical properties due to the radiotherapy.

The initial inputs of their model are MRI images of the patient in prone position. The gravity is reversed to work in an unloaded position. Then, the tumor and the negative margins are virtually removed. At that point, some mechanical parameters need to be set: the Young modulus (kPa), the density (kg/L) and the Poisson ratio. By adding gravity, we get the shape of the breast just after surgery and in the standing position, which is the most natural position. Thanks to the mechanical model, the dot product of the stress vector and the strain vector can be computed in the x-, y- and xy-direction [11]. Afterward, we needed to model the shape of the breast during the healing process. Therefore, a cellular automata model was

implemented to simulate the healing process. The agent-based model was computed with zero gravity because:

- the surgery is done virtually which means without external parameters (i.e gravity).
- the agent-based model was built on the assumption that the cell arrangement is not affected by gravity. The only external considered parameter is the stress that is estimated in the mechanical simulation.

At the end of this step, an updated geometry of the breast was given. However, seeing that the healing process is really slow, the loop had to be closed on the mechanical model. The shape of the cavity changes during the process and so does the shear stress on the wound. Figure 1.2 schematizes the main ideas of the shape prediction.

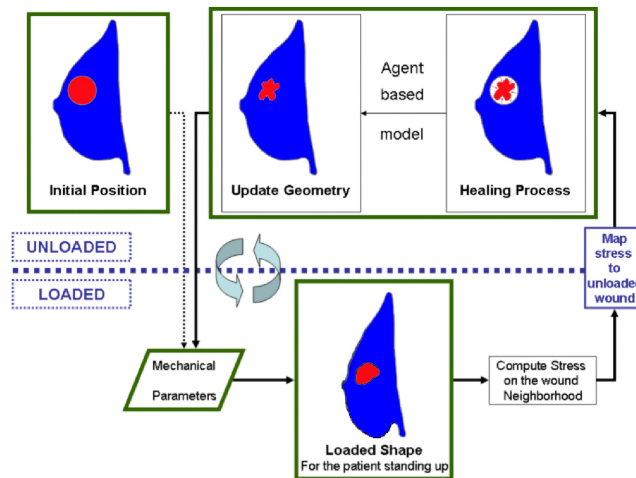


Figure 1.2: Steps to model the shape of the breast after BCT, from [25]

R. Salmon et al. [11] improved this prediction model by understanding the effects of

radiotherapy on the shape of the breast.

The final aim of our common project is to develop a Virtual Surgery Toolbox to help surgeons by transitioning our simulation data into clinical data.

1.3 Objective of our work

A lumpectomy is a procedure in which a surgeon removes the tumor with a circumferential margin of healthy tissue. Although the recurrence rates after lumpectomy and mastectomy (removal of an entire breast) are almost similar (about 3% after mastectomy against 6% after lumpectomy) [3], patients seems less anxious about reoccurrence after mastectomy [4]. However, lumpectomy is much less invasive than mastectomy and its main advantage is that it preserves the appearance of the breast much more. According to the Quality of Life outcome [13], lumpectomy has more emotional and physical advantages than mastectomy because women do not permanently lose their breasts. Nevertheless, after undergoing a lumpectomy, the shape of the breast can show some defects such as asymmetries, concave deformities or distortions of the nipple-areola complex. M. Garbey et al. ([26] [11] [12]) conducted a study to design a Virtual Surgery Toolbox (VST) in order to predict the outcome of BCT before surgery. D. Thanoon et al. [25] and R. Salmon et al. [11] obtained reasonable results concerning the prediction of the shape of the breast. Thanks to these predictions, we would be able to improve the quality of life of the patient and to help the dialogue between the patient and the doctor. The objectives of this thesis are to determine if the theoretical results predict a realistic shape of the breast after

healing but also to fine-tune the model and to discover what are the key parameters. Our work focuses on the 3D reconstruction of the breasts of patients from our clinical study to assess the accuracy of the predictions and the analysis of the first patient data.

Chapter 2

State-of-the-art

The third dimension plays a decisive role in the analysis of dynamic or static objects. The ability to perform fast and accurate 3-dimensional (3D) reconstruction of an environment is central to many applications. In computer vision, people or objects can be tracked. This innovation is also expanded in the medical field. Indeed, motion can be analyzed like the respiratory gating. Over the past decades, this domain has seen an explosion of implementation due to this advancement.

The 3D modeling methods can be classified into two parts: active and passive systems. Active systems are systems that emit energy to retrieve information about the environment. The energy can be infrared light, electromagnetic or acoustic waves. On the other hand, a passive system only receives information from the surroundings without emitting any specific signal. These methods require vision sensors (e.g. CCD cameras) to restore the 3D shape [9].

In this part, for each type of systems, some 3D imaging technologies will be described.

2.1 Active systems

Active systems can be considered as a passive binocular stereoscopic system where one of the cameras is replaced by a light transmitter projecting a known pattern.

2.1.1 Structured light

For structured light, a transmitter replaces one of the cameras. A structured light 3D scanner projects a known light pattern into the 3D space [24]. This motif is then viewed by one or more cameras. The distortion of this pattern allows a reconstruction of the 3D environment. The system geometry is then retrieved via a calibration step in order to know the direction of the projected motif, the relative position between the transmitter and the receiver, and also the observed position. The 3D-coordinates are computed by an active triangulation method.

To sweep the object's total surface, the set consisting of the camera and the projector can be shifted or rotated. Thus, the resolution of this method depends on the scanning step, the projected pattern and also on the resolution of the camera. Often, this method's resolution is better than a stereoscopic system.

Such systems provide high resolution and accurate reconstruction. However, the scanning is not instantaneous which is a complication in our project given that we have to deal with breathing patients. Also, the projected pattern might be close to infrared light. There is a large population of dark skinned individuals in Houston and the increased light absorption with darker skin results in suboptimal reconstruction.

2.1.1.1 Microsoft Kinect

In the gaming area, a structured light device has been developed by Microsoft: the Kinect sensor as displayed in figure 2.1.



Figure 2.1: Kinect sensor developed by Microsoft from [17]

This sensor platform is a motion sensing system that features a RGB camera (to provide the color to the reconstruction) and a depth sensor, which consists of an infrared laser projector and a monochrome sensor. It generates 640×480 depth map at 30Hz.

Kinect works by projecting speckles in near infrared lights, which coincide with the known pattern. To be accurate, the calibration between the projector and the camera has to be known.

Each point has its corresponding speckle. Their size and shape depend on the distance and the direction to the 3D environment. The depth data are computed by the

triangulation of each speckle between the projected pattern and the pattern observed by the camera.

While this device is inexpensive, the acquired data are very noisy and contain many holes where no depth has been computed. Furthermore, we have to deal with motion blur when the device moves fast. The operation range is between 0.8 and 3.5m. This sensor was initially developed for the gaming arena. However, many applications have been developed around this tool. Yan Cui et al. [6, 7] proposed a method to capture a body model just using the Kinect sensor. To deal with the low resolution and the random noise of the camera, they implemented a super-resolution algorithm in which the color constraints were taken into account. Jing Tong also presented a scanning system to model human bodies. They used several Kinects to capture different parts of the scene [27]. Even so, their approach needs to consider the interference phenomena and misalignments in the registration steps.

2.1.2 Time-of-flight

Time-of-Flight (ToF) imaging refers to the measurement of the depth by quantifying the phase changes between the emitted light signal and the received once it bounces back from objects in the scene [14]. This is equivalent to determining the travel time between the source light emission and the received reflection. This method relies on the modulation and demodulation process. An infrared wave is directed to the target and the sensor detects the reflected light on the object.

For each pixel that encodes the depth map, the phase difference between the sent and the reflected waves is computed. Finally, the distance d to the object is calculated

as follows:

$$d = \frac{c}{2f} \frac{\phi}{2\pi} \quad (2.1)$$

where:

- $c = 3.00 \times 10^8 m.s^{-1}$ is the speed of the light,
- ϕ represents the computed phase difference,
- f corresponds to the signal frequency.

The quantity $\frac{c}{2f}$ is the maximum distance that can be measured without ambiguity. The main advantage of this method is the need for only one specific camera. Moreover, the high-energy light pulses are not sensitive to the background illumination. Nevertheless, there are several errors that occur (e.g., demodulation or integration time errors). The most critical error is motion blur caused either by the motion of the camera or by the movement of the captured object. Blurred regions in the depth image lead to distortions in the 3D reconstruction [21]. The cost of such a device was not appealing.

While motion results in unstable reconstruction, the team led by Christian Schaller achieved a system that gated the respiratory motion [23]. Simon Placht et al. introduced a solution to position patient during radiotherapy by implementing a registration framework [20].

2.2 Multiview stereoscopic reconstruction

A depth measurement can also be assessed from stereo matching by using multiple camera views. In this part, we will focus on binocular stereovision. Stereovision emulates human eyes.

Stereoscopy is a technique that reproduces the relief of a 3D world from at least two 2D images acquired at different angles. The reconstruction process will be clarified in section 4.1.

To achieve 3D construction using this method requires calibrated cameras [28]. The major problem of this approach is that some of the computational steps are extremely expensive. The image resolution depends on the density of points we are able to extract and significant image processing is needed to match stereoscopic pairs.

J. Salvi shows in his paper that the precision of the reconstruction depends on the calibration method that is implemented [22].

Chapter 3

Clinical Study

3.1 Protocol of the study

In order to achieve the validation of our model, Marlene Gilles et al. [13] set up a clinical study. This pilot study aims to compare the results of our multiscale model to the outcome of the surgical lumpectomy and the healing process. It involves 15 patients from Houston Methodist who were diagnosed with breast cancer and who will undergo lumpectomy followed by radiotherapy (i.e BCT). According to the clinical protocol, a woman can be part of this study if she meets these main criteria:

- be an adult female older than 30 years old.
- have an early stage, non-metastatic breast cancer.
- have received a pre-operative mammogram within 30 days of surgery.

- have received a pre-operative MRI within 30 days of surgery.
- will undergo a lumpectomy.
- will receive post-surgery radiotherapy (whole breast radiotherapy).

Once a patient gives her consent, she has a follow-up to observe and measure the changes of the shape of her breast that occurs during the healing process, from the surgery until six months after surgery. Therefore, at each meeting with the patient, several data acquisitions are performed. The time-line in figure 3.1 demonstrates when the patient will have her surgery and the regular follow-up visits to gather the data.

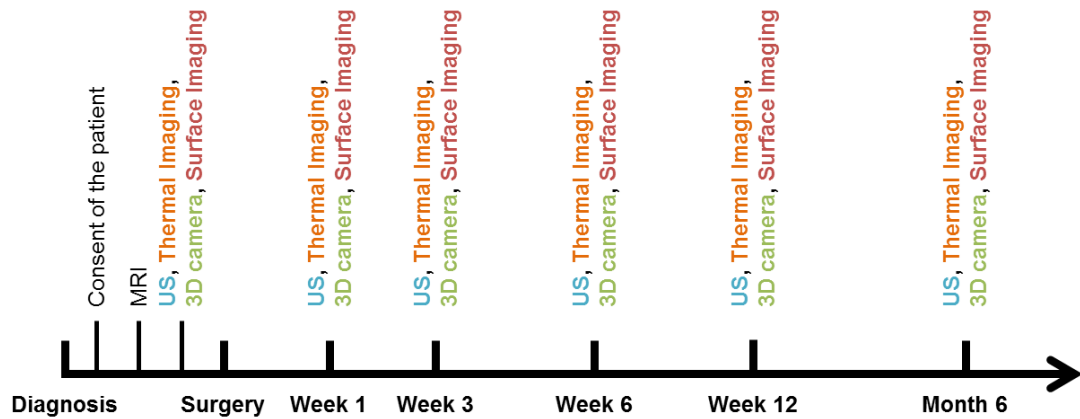


Figure 3.1: Clinical study time-line showing the follow-up and the acquired data

Many data are collected along these meetings and are saved into a database. The patients also all remain anonymous. For each patient and after every meeting, a worksheet is also updated.

3.2 Acquired data

3.2.1 MRI

Before surgery, a set of MRI images are acquired. These images are the reference of our mechanical model.

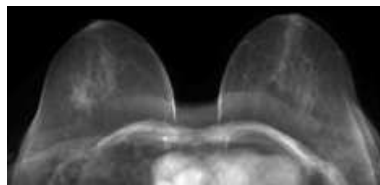


Figure 3.2: MRI image of the breasts in the transverse plane

The data set is processed to retrieve the 3D reconstruction of the breast as shown in figure 3.3.

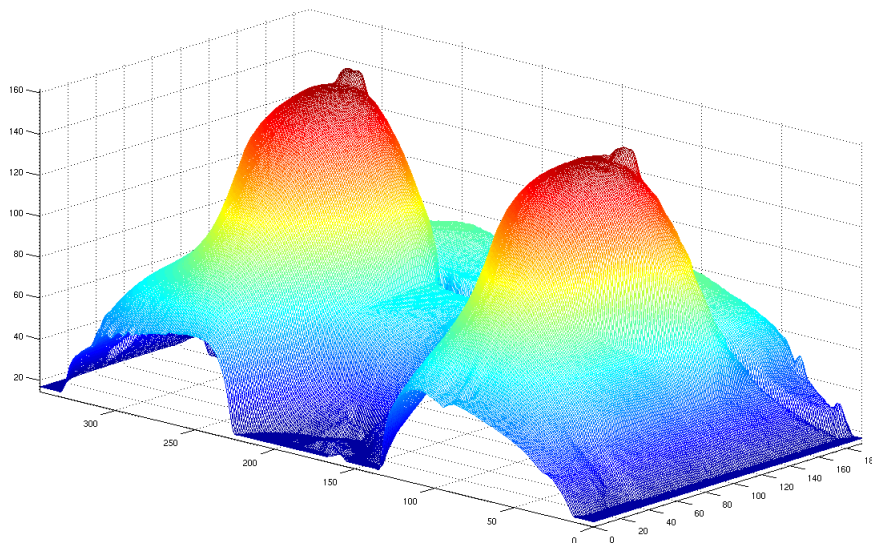


Figure 3.3: 3D surface reconstruction of the MRI data set

From these images, the distribution of tissues inside the breast is also extracted using

partially-supervised image segmentation techniques.

3.2.2 Ultrasound images

Breast ultrasound (US) is also performed to assess the changes of the cavity during the healing process.

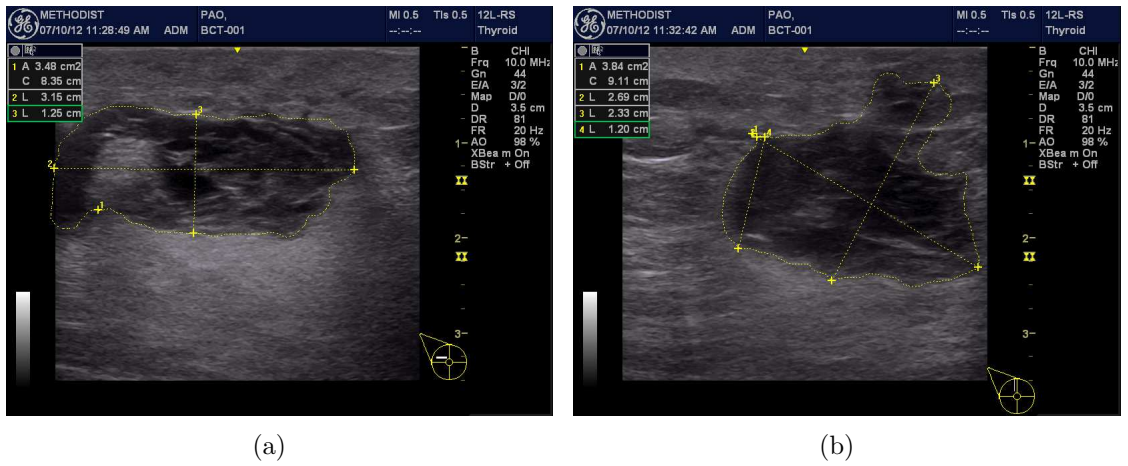


Figure 3.4: Example of US images (a) in transverse plane. (b) in coronal plane.

From the US images, the shape and the dimensions of the cavity and the position of the probe are extracted. These data are helpful in improving our healing model and to consider the effects of radiotherapy.

3.2.3 Thermal imaging

Inflammation makes tissue warmer because of a higher metabolic activity. Thus, thermal imaging via an E60 camera (figure 3.5(a)) was used to visualize the inflammation after surgery and to correlate it with the shape of the cavity. Every pixel of

such an image reports the temperature of the object at each particular point. The color map allows the user to understand visually what is happening.

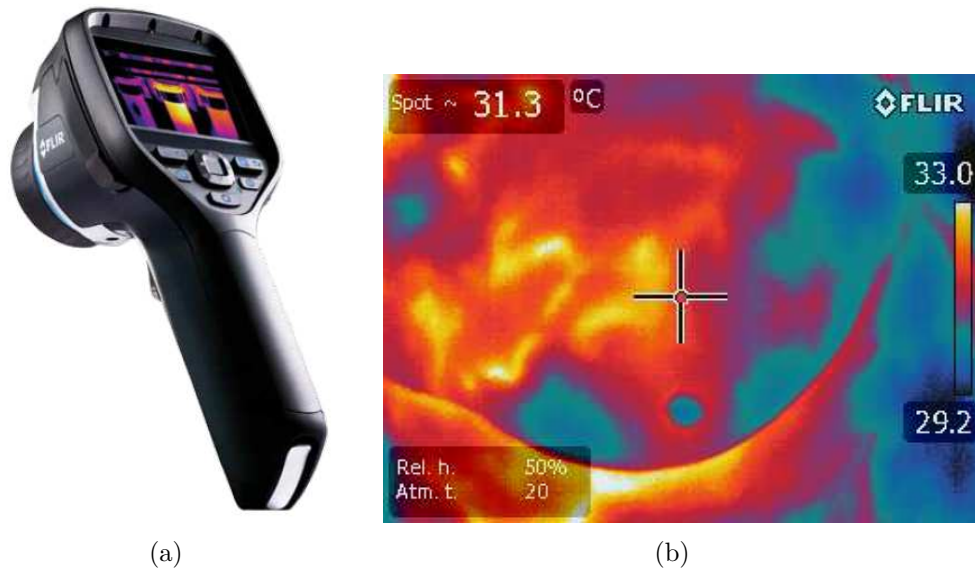


Figure 3.5: Thermal imaging. (a) E60 FLIR camera from [10]. (b) Picture of a breast taken with our E60 FLIR camera.

3.2.4 Surface imaging

A 3D-reconstruction of the breast is required to make a comparison between the predicted and the real shape of the breast after BCT. The first idea was to apply stereoscopy. Stereoscopy is a process that allows the reconstitution of three-dimensional images with two two-dimensional pictures of the same object but with a different perspective. The theoretical process is very simple, but unfortunately the practical part is much more difficult. Indeed, occlusions may appear.

We built a low-cost stereoscopic system. It is made up of two D70s Nikon cameras

along with a video projector and a laptop to project black and white stripes.



Figure 3.6: Our stereoscopic system made up of two cameras, a videoprojector and a laptop

During my Master's thesis, we mainly focused on the 3D-reconstruction from the images acquired with the stereoscopic system. The steps to reconstruct the surface are explained in chapter 4.

3.2.5 Quality of life

At each visit, the patient has to fill out a quality of life form where she has to assess, among other things, her pain.

Chapter 4

3D Reconstruction

In chapter 2, we discussed the different approaches to achieve a 3D-reconstruction. For our project, the adopted method needed to be both cost effective and mobile. Indeed, any doctor should be able to manipulate the set-up in the standard room where they meet patients. Therefore, our choice was to work with a stereoscopic system. However, we have to deal with:

- the scar after surgery,
- the colour of the skin (which is uniform),
- reflections on the skin,
- mobility of the patient because of breathing,
- hidden surfaces.

4.1 Background

A stereoscopic reconstitution is a process that allows us to assess the third dimension from a stereoscopic pair of images. This technique is divided into three main stages. First, the system is calibrated to determine the intrinsic and extrinsic parameters. Then, points from one view have to be matched to points from the other view. Lastly, the 3D-coordinates need to be computed.

4.1.1 Coordinate systems

To compute the 3D-coordinates, three different coordinate systems are used:

- (X, Y, Z) , the 'real' coordinate system,
- (x, y, z) , the camera coordinate system,
- (u, v) , the image coordinate system.

Homogeneous coordinates are employed because they are more relevant in projective geometry and allows us to define a transformation between two frameworks with a matrix multiplication. Table 4.1 discerns the Cartesian coordinates from the projective coordinates for a coordinates vector, a rotation and a translation matrix.

	Cartesian coordinates	Homogeneous coordinates
Used in	Euclidian geometry	Projective geometry
3D-coordinate vector	$\begin{pmatrix} x \\ y \\ z \end{pmatrix}$	$\begin{pmatrix} x \\ y \\ z \\ 1 \end{pmatrix}$
Rotation matrix	$\begin{pmatrix} r_{11} & r_{12} & r_{13} \\ r_{21} & r_{22} & r_{23} \\ r_{31} & r_{32} & r_{33} \end{pmatrix}$	$\begin{pmatrix} r_{11} & r_{12} & r_{13} & 0 \\ r_{21} & r_{22} & r_{23} & 0 \\ r_{31} & r_{32} & r_{33} & 0 \\ 0 & 0 & 0 & 1 \end{pmatrix}$
Translation matrix	$\begin{pmatrix} t_X \\ t_Y \\ t_Z \end{pmatrix}$	$\begin{pmatrix} 1 & 0 & 0 & t_X \\ 0 & 1 & 0 & t_Y \\ 0 & 0 & 1 & t_Z \\ 0 & 0 & 0 & 1 \end{pmatrix}$

Table 4.1: Comparison between Cartesian and homogeneous coordinates for transformation matrices

4.1.2 Calibration

Calibration of the stereoscopic system is a crucial step where the relation between the real world and the digital image coordinates is estimated. The accuracy of this phase will highly affect the final 3D-reconstruction. First and foremost, the intrinsic parameters are computed. They characterize the mapping of an image point from camera to image coordinates in each camera as follows:

$$\begin{pmatrix} u \\ v \\ 1 \end{pmatrix} = \begin{pmatrix} f_X & 0 & c_X \\ 0 & f_Y & c_Y \\ 0 & 0 & 1 \end{pmatrix} \begin{pmatrix} x \\ y \\ 1 \end{pmatrix} = A \times \begin{pmatrix} f_X & 0 & c_X \\ 0 & f_Y & c_Y \\ 0 & 0 & 1 \end{pmatrix} \quad (4.1)$$

where:

- f_X and f_Y represent the focal lengths in pixel units,

- c_X and c_Y express the optical center of the camera,
- A is called the camera matrix.

Then, the extrinsic are gauged. They describe the relative position and orientation of the two cameras. This rigid transformation is given by 4.2.

$$\begin{pmatrix} x \\ y \\ z \\ 1 \end{pmatrix} = \begin{pmatrix} r_{x/x} & r_{x/y} & r_{x/z} & t_x \\ r_{y/x} & r_{y/y} & r_{y/z} & t_y \\ r_{z/x} & r_{z/y} & r_{z/z} & t_z \\ 0 & 0 & 0 & 1 \end{pmatrix} \begin{pmatrix} X \\ Y \\ Z \\ 1 \end{pmatrix} \quad (4.2)$$

where:

- the r-coefficients represent the rotation matrix,
- the t-coefficients describe the translation matrix.

Finally, we access the pinhole camera model. Equation 4.3 characterizes this model.

$$\begin{pmatrix} u \\ v \\ 1 \end{pmatrix} = \begin{pmatrix} f_X & 0 & c_X \\ 0 & f_Y & c_Y \\ 0 & 0 & 1 \end{pmatrix} \begin{pmatrix} r_{x/x} & r_{x/y} & r_{x/z} & t_x \\ r_{y/x} & r_{y/y} & r_{y/z} & t_y \\ r_{z/x} & r_{z/y} & r_{z/z} & t_z \end{pmatrix} \begin{pmatrix} X \\ Y \\ Z \\ 1 \end{pmatrix} \quad (4.3)$$

This model is equivalent to:

$$\begin{pmatrix} x \\ y \\ z \end{pmatrix} = R \times \begin{pmatrix} X \\ Y \\ Z \end{pmatrix} + t \quad (4.4)$$

$$x' = \frac{x}{z} \tag{4.5}$$

$$y' = \frac{y}{z} \tag{4.6}$$

$$u = f_X \times x' + c_X \tag{4.7}$$

$$v = f_Y \times y' + c_Y \tag{4.8}$$

However, real lenses usually present some distortions. Therefore, the above model is extended by adding radial and tangential distortion coefficients [2].

To solve the system of equations, we can use a chessboard because:

- its geometry is well-known. To figure out the position of a corner, we need to know the number of rows and columns the chessboard has and the size of each square.
- its corners are easy to detect thanks to computer vision algorithms.

4.1.3 Point matching

The next and most difficult challenge consists of searching for correspondences in a stereoscopic pair. Some occlusions may appear: a 3D point is only depicted in one image, an object can hide another one in one of the views, points can be in a different order and distance changes from one image to the other. Imprecise mapping leads to an erroneous 3D-reconstruction. Many algorithms have been implemented to match points from both images. Among these methods, one solution would be

to extract features points (e.g., corners) from both images and to match them [33]. Another technique suggests a correlation method. A rectangular window is shifted in the image and the most relevant window in the second image is sought by looking for the maximum correlation between both windows [15].

Our stereoscopic system is calibrated so that the epipolar constraint can be applied. Epipolar geometry is a notable tool and is summarized in figure 4.1.

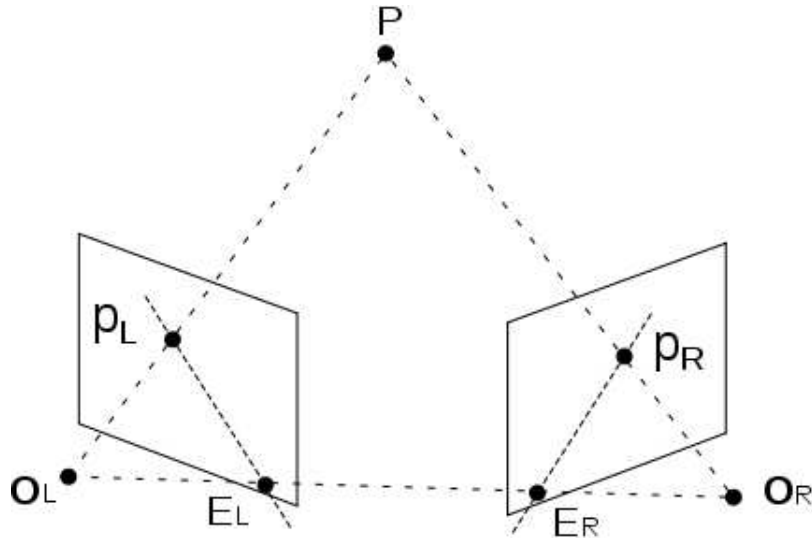


Figure 4.1: Pattern illustrating the different notions in epipolar geometry from [34]

According to [31], an epipole is the center of projection from one camera projected in the image plane of the other camera. The projection centers O_L and O_R (i.e. optical center of each camera) and the point P from the scene define the epipolar plane. Epipolar lines are the intersection of the epipolar plane with the image plane. The epipolar constraint assures that corresponding points are constrained to lie along conjugate epipolar lines. Thus, this reduces the search from 2D to 1D. The point matching can still be simplified by rectifying the stereoscopic pair. Each image is

subject to a transformation such that epipolar lines become collinear and parallel to the x-axis of the image, which is equivalent to map epipoles to infinity. So, for each point of the left image, we just need to look along the same row in the right image.

4.1.4 Computation of the 3D-coordinates

Once the images are rectified and the mapping finished, the passive triangulation method provides the 3D-coordinates as shown in figure 4.2.

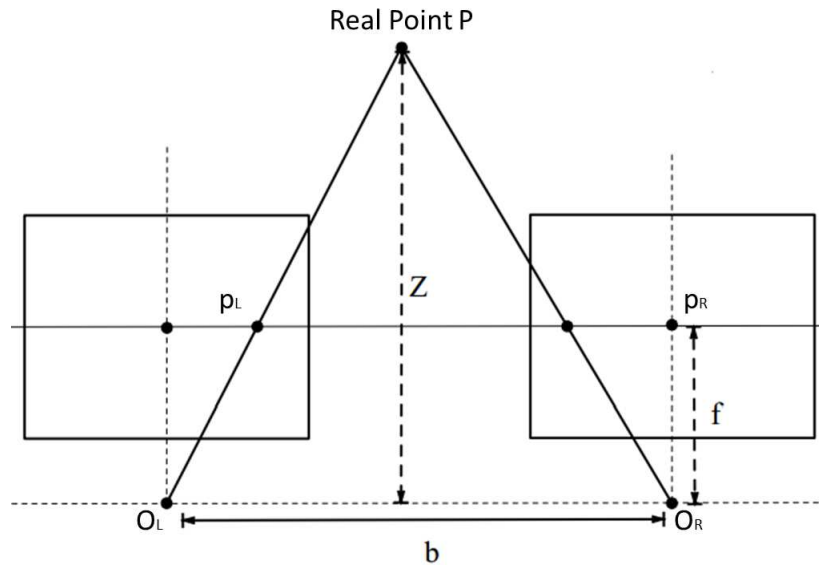


Figure 4.2: Geometry to compute the 3D-coordinates thanks to the triangulation method

This geometry provides the following equations:

$$X = \frac{x_L Z}{f} = \frac{x_L b}{d} \quad (4.9)$$

$$Y = \frac{y_L Z}{f} = \frac{y_L b}{d} \quad (4.10)$$

$$Z = \frac{bf}{d} \tag{4.11}$$

where:

- (x_L, y_L) are the coordinates of the real point P projected on the left image,
- (x_R, y_R) are the coordinates of the real point P projected on the right image,
- (X, Y, Z) are the coordinates of the scene point P,
- f represents the focal length,
- b , called baseline, describes the distance between both centers of projection,
- $d = x_L - x_R$ (disparity) is the relative difference in the location for a common object projected on the two views.

This technique is similar to the human vision and is implemented for many other instruments.

4.2 Improvements on the stereoscopic reconstruction

The classical approach of stereoscopic restitution needs to be improved for our project. The skin of patients is uniform so the mapping process would have been almost impossible. Being inspired by the idea of structured lighted [16], we decided to project vertical stripes on the patient in order to match points in a more accessible

approach. Thus, the main idea was to first take pictures of a chessboard to calibrate our stereoscopic system. Next, these vertical stripes were projected on the patient's body thanks to a video projector and pictures of this scene were then acquired. These lines involved an image processing step in which they were segmented. Afterwards, the mapping procedure and the 3D-coordinates computation are set up. Finally, another image processing was added because of too noisy results. We simultaneously worked with patients data and mannequin images.

The image processing was implemented under Matlab while the calibration and the 3D-reconstruction were implemented in C++ using OpenCV [2]. OpenCV is an open source library that offers appropriated and well-documented functions for computer vision. For example, *findChessboardCorners()* locates the corners of the chessboard in a grayscale or color image and returns a value depending on if all the corners have been detected or not. The surfaces are displayed under Gmsh which is a finite element software.

4.2.1 Preprocessing

The major challenge was to handle image processing tools to segment the projected stripes. A simple threshold would not suffice as long as this is not robust at all.

In this section, the different implemented methods that lead us to a reasonable technique are described.

4.2.1.1 Difference of Gaussians approach

Introduced by Marlene Gilles [13], the very first idea was to perform the Difference of Gaussians (DoF) algorithm on the images. This method is a well-known and commonly employed edge-detection filter where one smoothed version of the original images is subtracted to another smoothed version (figure 4.3).

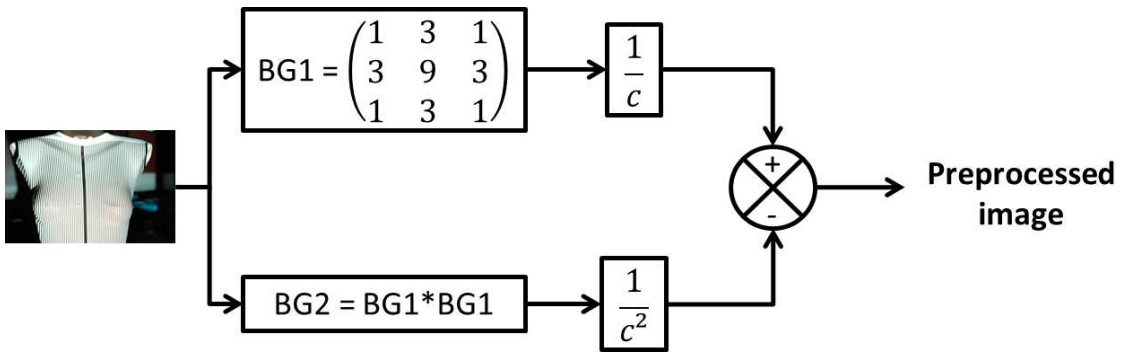


Figure 4.3: Difference of Gaussians filter implemented to detect the projected lines

Each blurred image is computed by convolving the original grayscale image with a Gaussian filter having a specific radius. According to the size of both radii, different results are expected. Our figures are light on a dark background so the second radius needs to be higher than the first one. A Gaussian filter removes high frequency information of an image so this DoF approach is equivalent to a band-pass filter that keeps only a range of spatial frequencies.

c is a coefficient to adjust as the image may be. A threshold is defined and the preprocessed image is then binarized.

This method was working well on the mannequin. Nevertheless, it was not robust enough while dealing with the patient images. The skin reflected the light but also presented some shadows. Furthermore, the projected lines appear discontinuous just

under the breast in the patient images.

4.2.1.2 Improved Difference of Gaussians

The first and minor problem was the discontinuities of the lines. To fix it, the top part of the chest was manually segmented by following the curve describing the discontinuities. The 3D-reconstruction of the top part was enough.

The predominant drawback of the previous method was the intensity of the light which varied from one part of the patient's chest to another as displayed in figure 4.4.

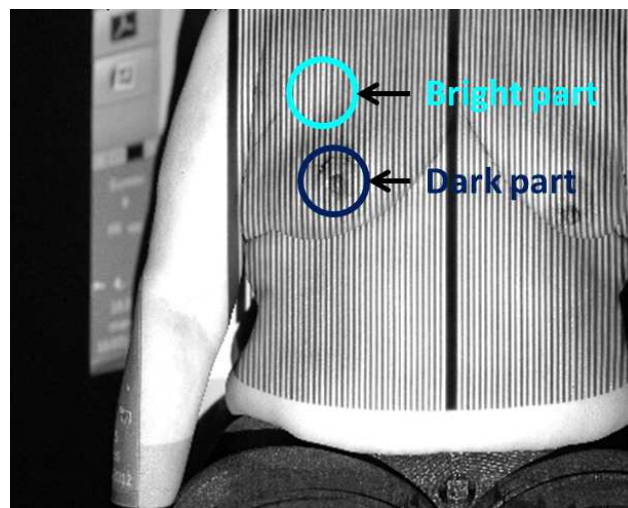


Figure 4.4: Image presenting high variations of light intensity, the cyan circle gives an example of a bright part while the dark blue one reveals a dark part

Therefore, three parts were discerned in the segmented chest by defining two different thresholds as established in the following histogram (figure 4.5).

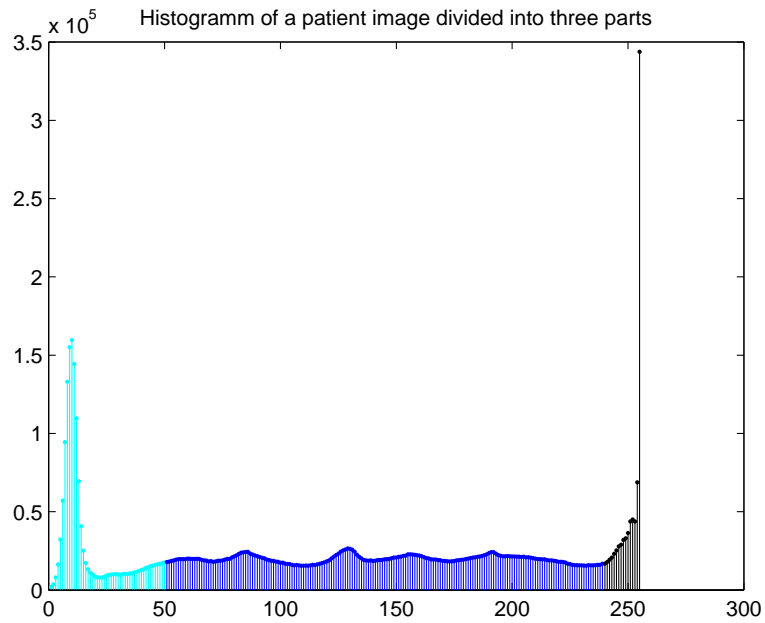


Figure 4.5: Histogram marking the thresholds in order to cut the image out different parts

Then, we kept the same idea by processing every distinct part with the DoG algorithm that we analyzed above. The c coefficient needed to be fine-tuned independently for each part. Last, the three parts were assembled together to obtain the final result.

Overall, the line detection gave good results. However, some misdetections remained because of the scar, the nipples, and also due to beauty spots or landmarks for the radiotherapy (blue crosses drawn on the patient's body).

4.2.1.3 Active contour method

Our goal was a segmentation problem in which the projected lines needed to be detected. Segmenting an image consists in separating objects or regions of interest from the background. A region of interest Ω is described by:

- a local descriptor which characterizes the boundary of Ω (e.g., minimal length, curvature),
- a global descriptor which outlines Ω as the mean or the standard deviation of the region.

An active contour (so-called "snake") is a dynamic system composed of mobile nodes such that the curve described by these points evolves until equilibrium is found. Therefore, an energy function is defined in such a way that the minimum of this function is equivalent to the boundary of the region of interest.

The energy function is often determined to segment regions defined by gradient. However, Tony Chan et al. [5] proposed a new model to detect objects that does not depend on the gradient of the image. The energy is no longer just the sum of the intern and extern energies but add some regularizing terms as introduced in equation 4.12.

$$F(C, c_1, c_2) = \mu \cdot \text{length}(C) + \nu \cdot \text{area}(\text{inside}(C)) \\ + \lambda_1 \int_{\text{inside}(C)} |u_0 - c_1|^2 dx + \lambda_2 \int_{\text{outside}(C)} |u_0 - c_2|^2 dx \quad (4.12)$$

where:

- u_0 is the image,
- C is the curve that has to fit the boundaries of the region of interest,
- c_1 (respectively c_2) is a constant computed as the average of u_0 inside C (respectively outside C),
- μ , ν , λ_1 and λ_2 are fixed parameters.

To solve the problem, the energy is formulated in level set [29]. The solution is obtained after the equation was discretized using an finite differences implicit scheme. Since the topology of the stripes was known and this method does not change the topology, the curve was initialized as perfect vertical lines. Afterwards, a time step loop was implemented that computed the perimeter and area inside the curve and the average value of the image function inside and outside the curve in order to figure out at each iteration the new contour.

The results of the segmentation were reasonable even if there were still some misdetection remaining in very dark parts of the image. However, this idea was dropped because of the computation time which was too long in comparison to the quality of the output.

4.2.1.4 Signal processing

In order to figure out how to deal with the scar and other marks on the patient's body, we had to approach the problem from a different perspective. By displaying a cross section of the acquired image, the light saturates in the middle of the image

and the further the pixel is from the middle, the lower its intensity is (figure 4.6).

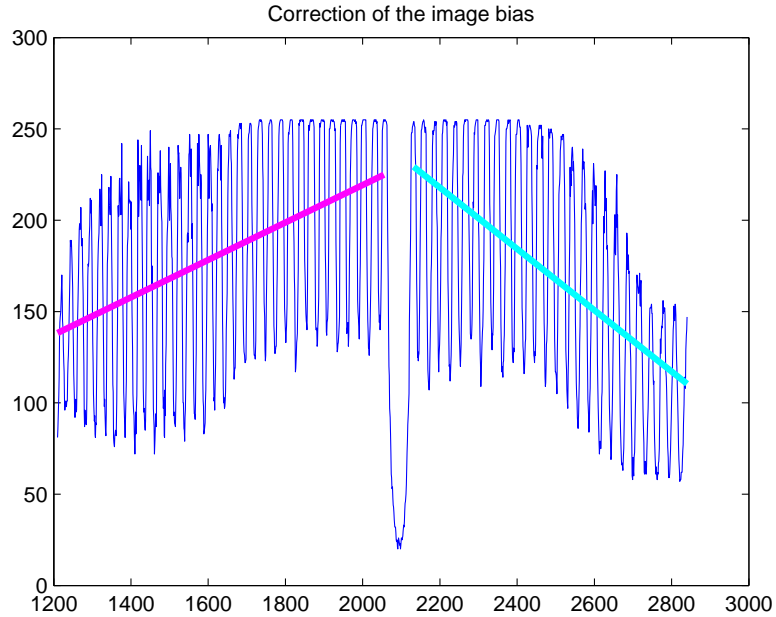


Figure 4.6: Cross-section of a common acquired image proving the intensity of the light is not uniform

This phenomenon appears because of the video-projector. The intensity of the light is usually concentrated in the middle of the beam and decreases when the distance to the center increases. This explains how a simple threshold could not work. To balance this outcome, the image bias was corrected. Thus, the slope of the signal on either side of the large black line was computed. In figure 4.6, the magenta line (respectively the cyan line) shows the slope on the left side (respectively on the right side). Then, the intensity of each pixel of the image was corrected such that the slope becomes horizontal.

This solution is a great start because the overall detection gave reliable results. Nonetheless, the dilemma of the detection around the nipples, at the scar location

or at some other spots on the skin was not settled.

While bearing in mind signal processing, an analogy between a temporal signal and a spatial signal (i.e., the image) was conducted. Indeed, the projected lines on the image could be interpreted as an ideal periodic rectangular signal. The Fourier Transform (FT) for the rectangular function is a sine cardinal (sinc). The Fourier Transform is defined by:

- in 1D:

$$F(\nu) = \int_{-\infty}^{+\infty} f(t)e^{-i2\pi\nu t} dt \quad (4.13)$$

- in 2D space over an x-y plane:

$$F(u, v) = \int_{-\infty}^{+\infty} \int_{-\infty}^{+\infty} f(x, y)e^{-i2\pi(ux+vy)} dx dy \quad (4.14)$$

The result of the Fourier Transform on a characteristic images we deal with is shown in figure 4.7. The black circle on the plot coincides with the main spike of the sine cardinal in 1D.

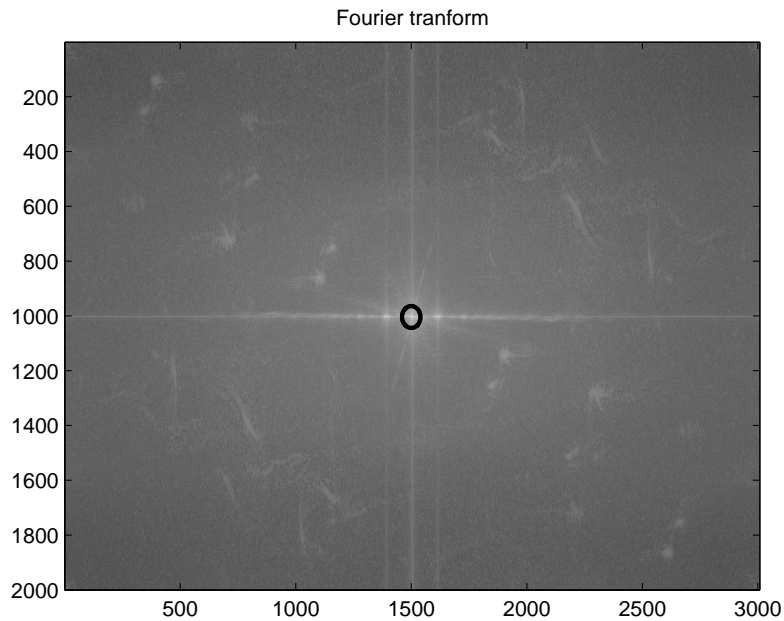


Figure 4.7: Result of the Fourier Transform on the image where the black circle exhibits the main spike of the sinc

The edge of the signal is equivalent to high frequencies in the Fourier domain. The idea was to delete as much as possible the projected lines and hence, to construct a high pass filter. Consequently, high frequencies of the temporal signal were set to zero, which conformed with a simple Gaussian function. The corresponding frequencies in the image were as well set to zero. Finally, the Inverse Fourier Transform (IFT) was applied on both signals. The IFT of a Gaussian is also a Gaussian which explains the blurred image reached by computing the IFT of the image FT after removing high frequencies as exposed in figure 4.8.

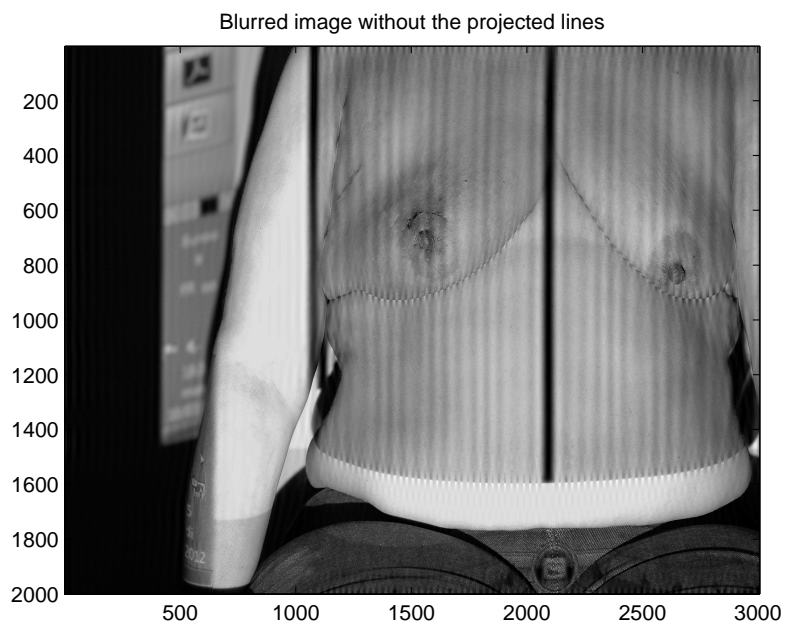


Figure 4.8: Blurred image accessed after eliminating unwanted frequencies in the Fourier domain

The subtraction of the above result to the original grayscale image matched with a high pass filter and gave us the following result (figure 4.9).

A last threshold provides the final segmentation of the stripes looking at the cross-section at the level of the patient's nipples in figure 4.10.

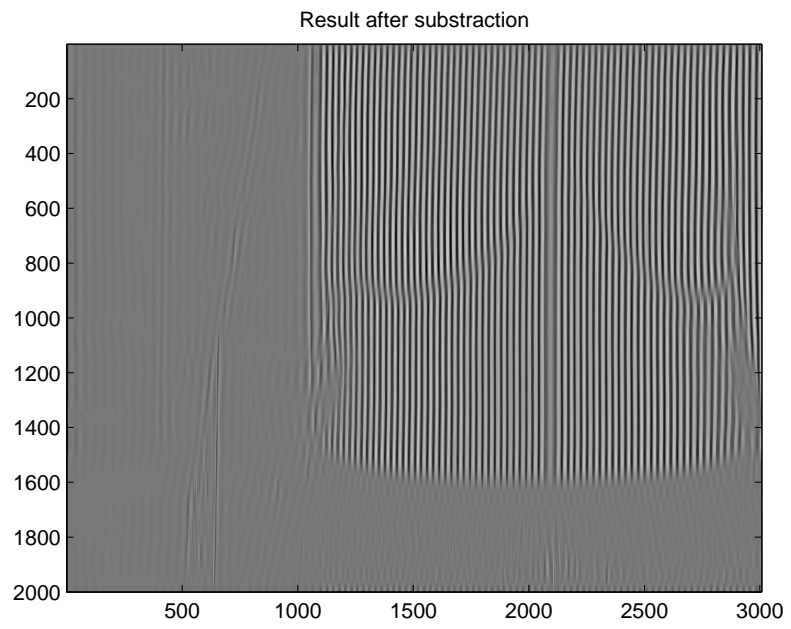


Figure 4.9: Results of the images subtraction that afford a clear image to process

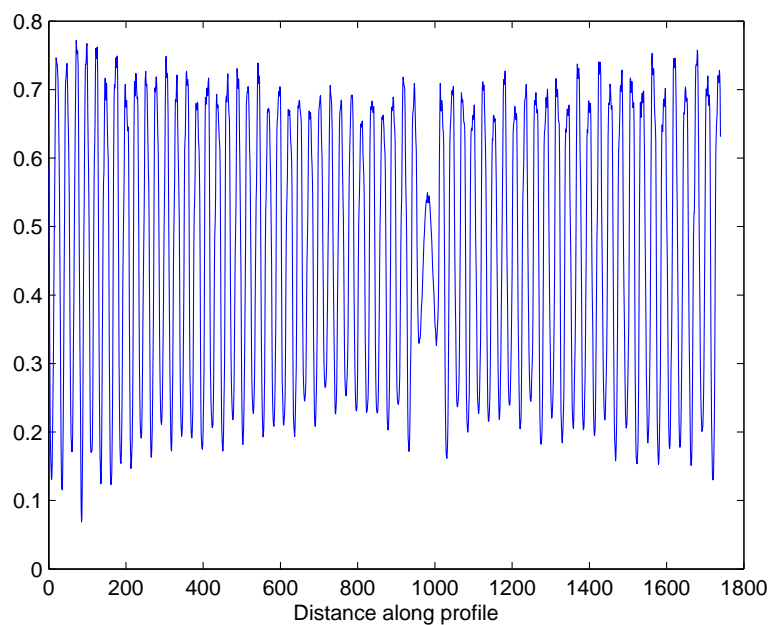


Figure 4.10: Cross-section after subtraction at the level of the nipples proving a threshold is sufficient to segment properly the lines

This observation produced excellent line detections but needed to be refined in terms of image filtering.

The most convenient and similar filter that we noticed is called the Gabor filter [30] known as an edge detection filter in image processing. This filter is a linear filter whose impulsion response is a sine curve modulated by a Gaussian. The goal of this filter is to pick out, in the Fourier domain, the set of frequencies which pattern the region of interest. Figure 4.11 demonstrates the outcome of this filter. Again, a threshold provides the final segmentation.

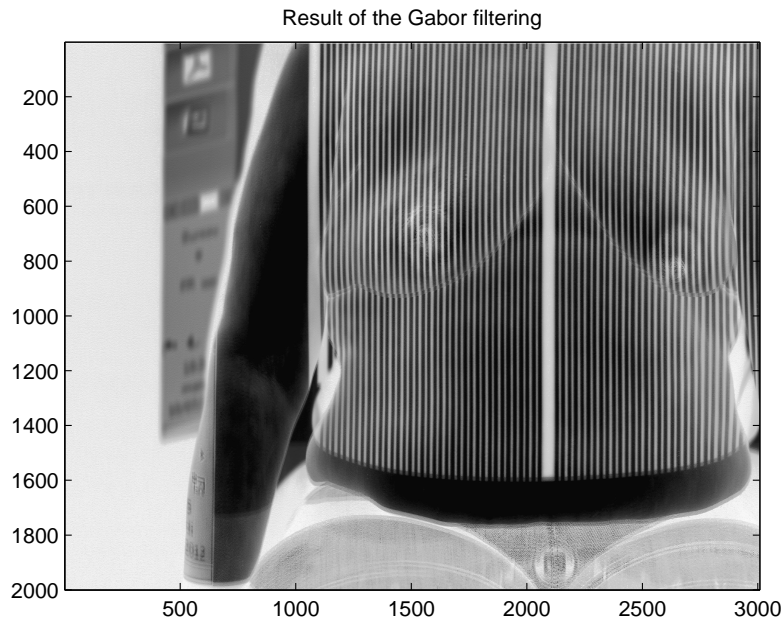


Figure 4.11: Achieved image after applying the Gabor filter

4.2.2 3D coordinates computation

The inputs of our 3D coordinates computation are the above processed images. First, these images were rectified in order to reach parallel and horizontal epipolar lines. As explained in section 4.1.3, this rectification reduced the degree of complexity. A point of the left image and its corresponding point in the right image are on the same horizontal line which means that they have the same y-coordinate. The green lines in figure 4.12 are horizontal. The left image shows an unrectified pair of images while they were rectified on the right image.

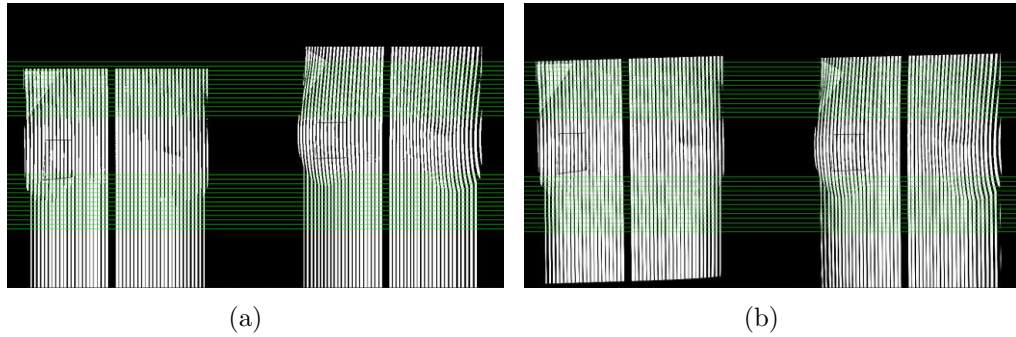


Figure 4.12: Image rectification (a) Unrectified stereoscopic pair (b) Rectified stereoscopic pair pointing out two matched point have the same y-coordinate.

In order to map stereoscopic pairs from the two images, a landmark was exploited. The position of the largest black projected line was gauged. Then, we assumed that the closest line from the landmark on the left image was also the closest from the landmark on the right image and so forth. This hypothesis allowed us to simplify the most delicate part.

From the known intrinsic and extrinsic parameters of our stereoscopic system, the 3D-coordinates were computed as explained in paragraph 4.1.4.

4.2.3 Postprocessing

Unfortunately, our point cloud may be noisy. The reconstruction was smooth and so equivalent to low frequencies in the Fourier domain while the noise coincided with high frequencies. Therefore, the following low-pass filter was computed [8] to remove the noise.

$$\sigma(\xi) = y^4(35 - 84y + 70y^2 - 20y^3) \quad (4.15)$$

where $y = 0.5(1 + \cos(\pi\xi))$.

The best way to compute it was to work in the frequency domain. Therefore, the Discrete Fourier Transform was applied on our discretized signal. Equation 4.16 shows the definition of the Discrete Fourier Transform.

$$F(k) = \sum_{n=0}^{N-1} f(n) * \exp(-2i\pi k \frac{n}{N}), 0 \leq k < N \quad (4.16)$$

where:

- f is the signal, and
- N is the sampling number.

Then, we needed to create a periodic signal by respecting the Dirichlet boundary condition before applying the filter. We finished by coming back to the spatial domain thanks to the Inverse Discret Fourier Transform.

The final reconstructed surfaces were plotted under Gmsh which is a finite element software.

Chapter 5

Results and discussion

5.1 3D-reconstruction

From the image processing steps, we were able to collect 3D-reconstructions of the patient and the mannequin as displayed in figure 5.1 and 5.2.

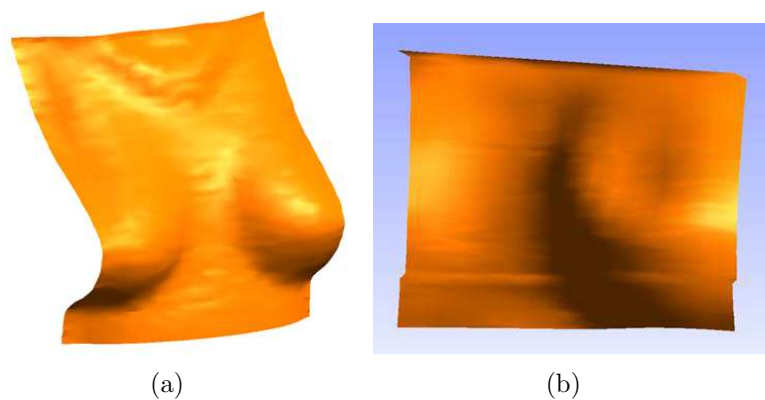


Figure 5.1: Results for the mannequin 3D-reconstruction (a) Overall view (b) View showing the artificial defect on the breast

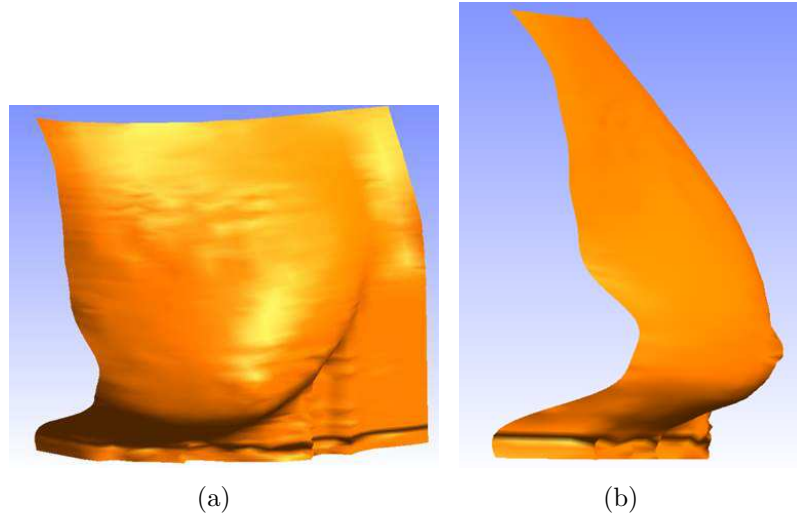


Figure 5.2: Results for the patient's right breast 3D-reconstruction (a) in the coronal plane (b) in the sagittal plane

The quality of the results was not only evaluated for accuracy but also according to the visual appearance. As seen in figure 5.1(b), the defect artificially added on our mannequin was clearly visible. No defect emerges from the patient's reconstruction because her surgery and subsequent healing did not lead to any cosmetic defect.

That does not mean that the precision of the reconstruction can be ignored. That is why a validation step has been design and will be explained in section 5.5.

5.2 Comparison with another system

Different systems able to provide a 3D-reconstitution of the patient (or mannequin) have been discussed in chapter 2. Given that the Kinect device is cheap, its noisy data easy to process, and that the area of gaming is expanding quickly, we opted for

Microsoft's equipment.

5.2.1 Kinect

The data collected from the Kinect were very noisy. When our clinical study was designed, this device had not advanced a lot. Despite this major drawback, this mechanism has been expanded in the gaming area and also used for many other applications.

RecFusion, an open-source software implemented by a German company, offers a solution to award a 3D-reconstruction. Their software is based on the KinectFusion approach with some modifications [19]. The depth images acquired from the Kinect are registered to the current 3D reconstruction using the Iterative-Closest-Point (ICP) algorithm. Once registered, the current 3D reconstruction is updated using the new depth measurements.

Before the acquisition, a voxel resolution can be fixed as well as the reconstruction volume. To get a reasonable reconstruction, the acquisition lasts at least 10 seconds during which the model has to turn around itself to allow a new view to the sensor. The tool can also be shifted to scan the whole model. When the reconstitution is complete, the scan is stopped. Then, a postprocessing is offered to change the mesh visualization, remove small disconnected parts or smooth the outcome.

Figure 5.3 provides two views of the mannequin reconstruction.

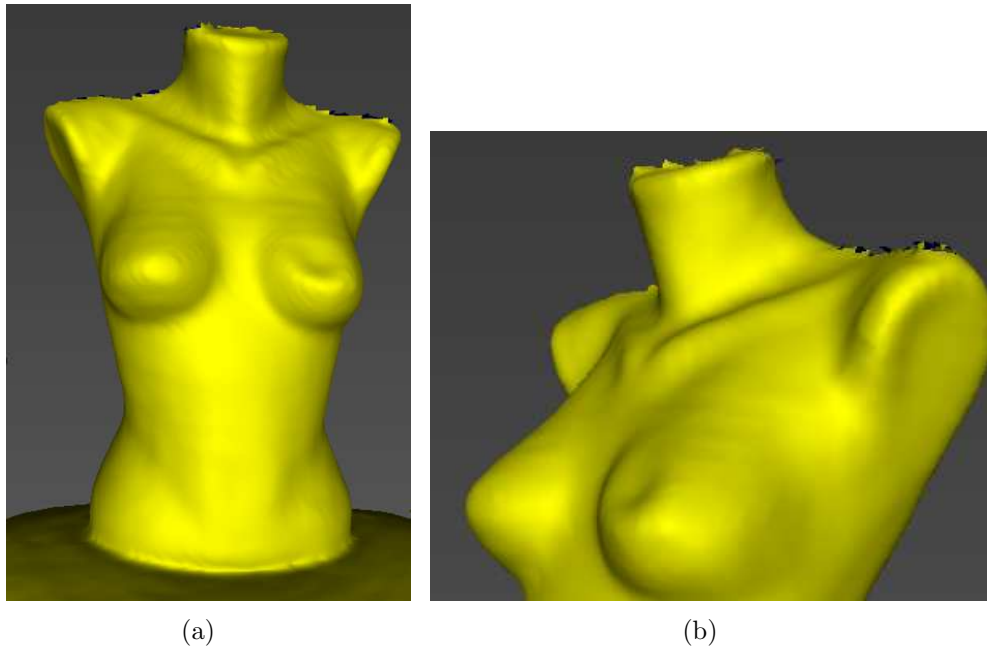


Figure 5.3: Reconstruction with Microsoft Kinect processed by RecFusion

5.2.2 Discussion

The 3D-reconstruction using the Kinect was explored to figure out if there was another system that would meet the specifications. It turned out that both systems seemed to be complementary. While the stereoscopic system appeared less accurate a priori, the Kinect needed to be placed at least at 80cm from the patient. Our stereoscopic system could be installed as close as wanted. The acquisition time was also a key factor. For the stereoscopic system, the acquisition is instantaneous. However, it took a few seconds for the Kinect to provide the mapping, which might bias the results for patients. Indeed, during the acquisition, the patient is breathing. Furthermore, the model was turning so these motions might affect the final reconstruction.

Finally, the depth map that the Kinect sensor computes is noisy. To correct these undesirable effects, the data were excessively smoothed which approximated the result and could remove some important patterns for us.

5.3 Validation

The validation process has been separated into two various steps.

5.3.1 Comparison of cross-sections in the sagittal plane

The first idea was to compare cross-sections in the sagittal plane for the mannequin reconstruction with the stereoscopic system and the Kinect sensor with the original mannequin. Thus, in all the cited instances, the contour of the cross-section was extracted. Distance ratio are also computed to fit the contours in the same framework as demonstrated in figure 5.4.

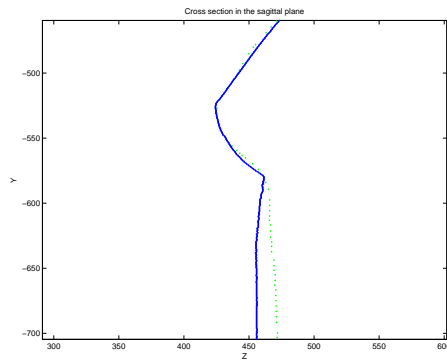


Figure 5.4: Comparison of the cross-section between the real mannequin (blue curve) and the Kinect reconstruction (green curve)

Thanks to these contours, we were able to rate the relative error of the two distinct reconstruction method. The one for the Kinect is smaller than the one for the stereoscopic system. This can be explain by the fact the stereoscopic provides a smaller resolution because of the width of the projected lines.

5.3.2 Accuracy of the stereoscopic system

To check how accurate our reconstruction was, a validation system was designed. It consisted of a regular grid and a laser whose accuracy is less than 1 millimeter as illustrated in figure 5.5.



Figure 5.5: Validation structure to gauge the accuracy of our stereoscopic system

Using the accurate laser, some distances from the grid to the mannequin will be measured. These points will be compared to the corresponding points in the stereoscopic reconstruction and we will be able to estimate the error and hence, the precision of the reconstruction.

The resolution of the reconstruction could also be determined. It can be at best

equal to the resolution of the input images if the matching step is fully dense which is difficult to acquire.

5.4 Analysis of the first patient data

The patient 1 was a female presenting a lobular carcinoma in-situ in the right breast. The tumor was described as an early-stage, non-metastatic tumor. The end of the procedure for our first patient allowed us to draw the initial conclusions.

First, figure 5.6 shows the time-line of operations on her as well as the acquired data. We can notice there is a gap between the protocol and the real schedule which can be partially explained by her chemotherapy. Indeed, patients involved in our clinical study should not receive this treatment but, with regards to her recovery, she was constrained to it.

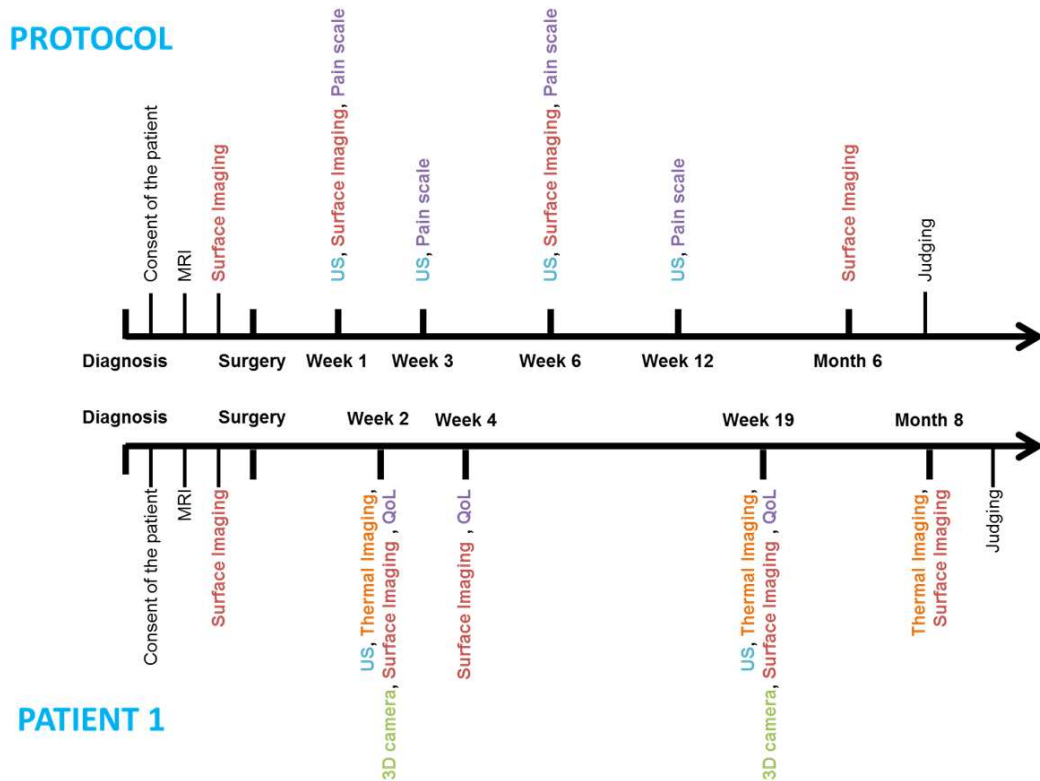


Figure 5.6: Comparison between the theoretical time-line of the protocol and the follow-up of our first patient

The images of the patient’s breast in frontal view allowed us to compute the difference of height between the left and the right nipple. The vertical positions of the nipple were measured in the image, rescaled using the calibration parameters and reported in the graph 5.7.

After surgery, this difference increased approximately 3 centimeters. During the chemotherapy period, the change in metabolic activity led to a decrease of her right breast (the one which underwent surgery). Finally, the effects of radiotherapy induce a new increase.

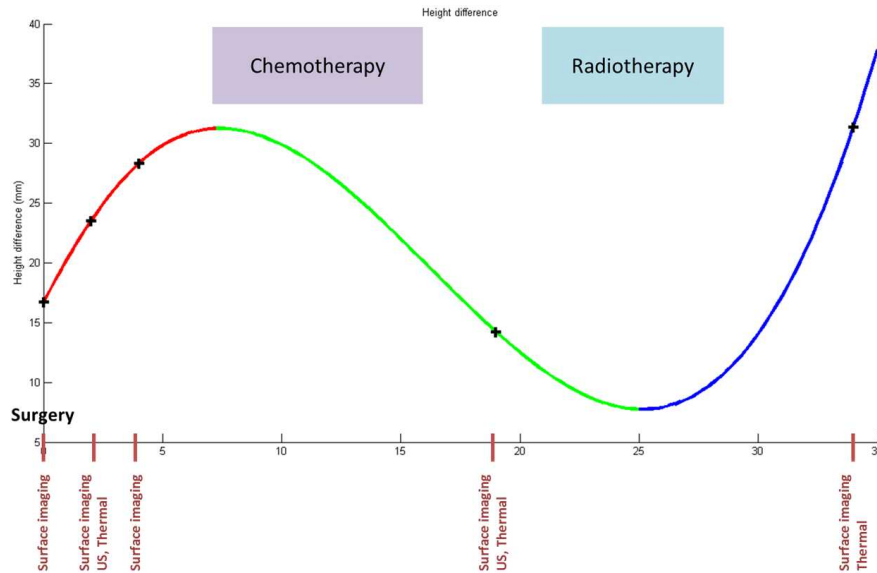


Figure 5.7: Difference of height between the two breasts during the healing process for our first patient

In the same way, the curve displaying the difference of area between both breasts was estimated (figure 5.8). Therefore, the cross-sections of both breast have been outlined from the data acquired during the follow up.

This contrast of area was significant after surgery and turned to zero after some weeks. At week 2 after surgery, we noticed an increase of volume of the breast by an order of magnitude of the size of actual cavity.

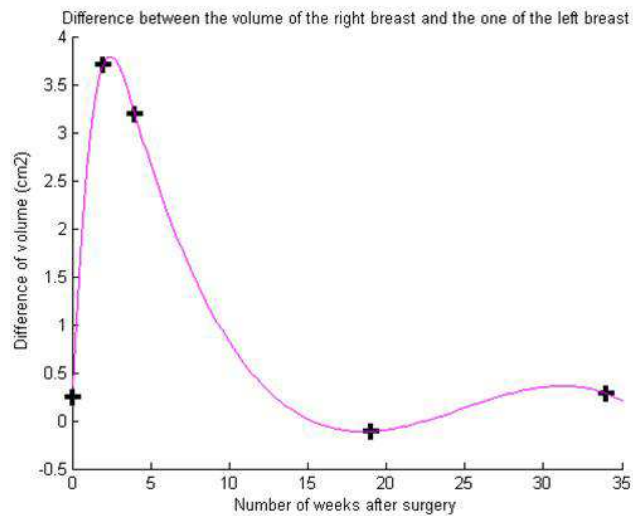


Figure 5.8: Evolution of the difference of volume between the two breasts during the healing process for our first patient

Finally, through thermal imaging, the temperature of the left and the right breast were measured and reported in the graph 5.9.

The temperature of the right breast was much higher than the one of the left breast just after surgery which can be interpreted by the inflammation of the breast. The difference of temperature tends to decrease even if the difference is still non zero at the end of the clinical study.

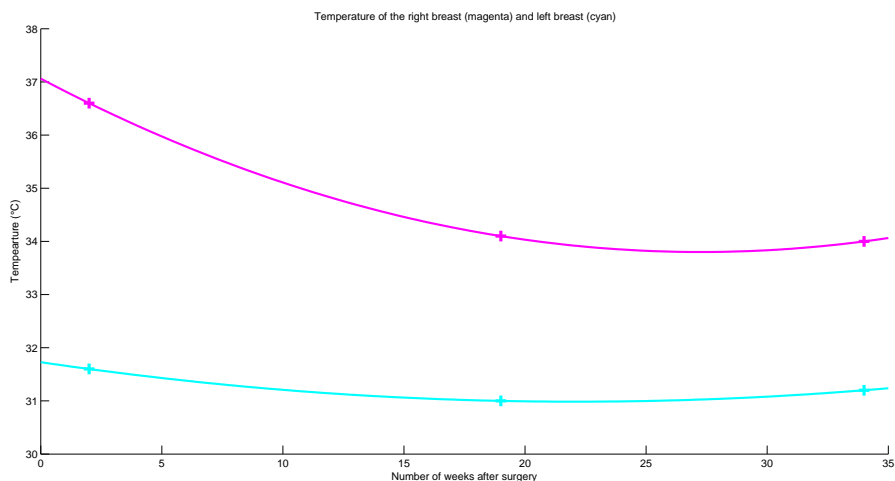


Figure 5.9: Evolution of the temperature for both breasts during the healing process for our first patient

The distinct points for the three previous graphs have been interpolated to get the curves. The lack of data between week 4 and 19 and between 19 and 34 might have modified the curves.

Despite some missing data, we could still interpret these curves. The healing process seemed to be divided into 3 stages:

- stage I from week 1 to 4 where the temperature of the right breast was much higher than the left one. Its volume increased and there was a high stiffness related to the inflammation.
- stage II from week 5 to 19. This was a recovery period and short time healing.
- stage III from week 20 to 35 during which the radiotherapy effects and the long term healing needed to be considered.

These observations allowed us to improve our model. In stage I, the volume increase was explained by adding seroma pressure effects while the anatomy shape changes were due to an increase of tissue stiffness. In stage II, the explanation may come from the absorption of seroma but still need to be computed. Ultimately, the last phase might be a repercussion of the radiotherapy on tissue stiffness.

Chapter 6

Conclusion

The primary goal of our project is to design a toolbox that provides a confident prediction of the shape of the breast for women undergoing Breast Conservative Therapy. This thesis focuses on the clinical study that has been set up to determine whether the predicted shape is realistic or not. Therefore, a 3D-reconstruction of the breast is required to be able to compare the real shape to the predicted one.

Two reconstruction systems are available: our stereoscopic system and Microsoft Kinect. Both structures are complementary while offering different benefits. The main achieved work was to reconstruct the breasts based on the images acquired with our own system. So, abounding image processing tools have been implemented in order to segment the projected lines. These lines could be misdeteected because of the reflection of the light on the skin, the presence of spots on the skin and the scar. Our first patient went through our clinical study. The acquired data allow us to calibrate the prediction model. They also lead us to suggest some changes into the

protocol. Indeed, more data are needed to understand better the behavior of the breasts during the healing process. Furthermore, the current data present some limitations. For instance, the breast is pressed on a plate during the MRI acquisition which introduces an error for the input of the model.

The next step of this project is to finish the validation in order to compute the accuracy of the reconstruction. Afterwards, the protocol needs to be discussed with the medical team and has to be improved before the new patients begin the study. Some cameras should also be added to our stereoscopic system to increase the vision field of the 3D-reconstruction. Finally, the new version of the Kinect sensor, slated to be released soon, may reduce the noise of the depth map and offer a better reconstruction.

Bibliography

- [1] American Cancer Society. *National Comprehensive Cancer Network, Breast Cancer, Treatment Guidelines for Patient*. September 2006.
- [2] Gary Bradsky and Adrian Kaehler. *Learning OpenCV*. O'Reilly Media, Inc., 1005 Gravenstein Highway North, Sebastopol, CA 95472, September 2008.
- [3] Breastcancer.org. Symptoms and Diagnosis. <http://www.breastcancer.org/symptoms>, 2013.
- [4] Abenaa M. Brewster, Gabriel N. Hortobagyi, Kristine R. Broglio, and et al. Residual Risk of Breast Cancer Recurrence 5 Years After Adjuvant Therapy. *Journal of the National Cancer Institute*, 100:1179–1183, August 2008.
- [5] Tony F. Chan and Luminita A. Vese. Active contours without edges. *Image Processing, IEEE Transactions*, 10:266–277, February 2001.
- [6] Yan Cui, Will Changz, Tobias Nölly, and Didier Stricker. KinectAvatar: Fully Automatic Body Capture Using a Single Kinect. In *11th Asian Conference on Computer Vision (ACCV 2012)*, 2012.
- [7] Yan Cui and Didier Stricker. 3D Shape Scanning with a Kinect. In *SIGGRAPH 2011*, Vancouver, 2011.
- [8] F. Dupros, W.E. Fitzgibbon, and M. Garbey. A Filtering technique for System of Reaction Diffusion equations. *International Journal for Numerical Methods in Fluids*, 52:1–29, September 2006.
- [9] El-Fathi El-Mejbri, Hans Grabowski, Harald Kunze, Ralf-Stefan Lossack, and Arno Michelis. 3D Reconstruction of Paper Based Assembly Drawings: State of the Art and Approach. *Graphics Recognition Algorithms and Applications*, 2390:1–12, 2002.

- [10] FLIR Systems, Inc. Flir. <http://www.flir.com/cs/emea/en/view/?id=41372>.
- [11] M. Garbey, R. Salmon, D. Thanoon, and B.L. Bass. Multiscale modeling and distributed computing to predict cosmesis outcome after a lumpectomy. *Journal of Computational Physics*, 244:321–335, August 2012.
- [12] M. Garbey, D. Thanoon, and B.L Salmon, R.and Bass. Multiscale Modeling and Computational Surgery: Application to Breast Conservative Therapy. *JSSCM*, 5:81–89, November 2011.
- [13] Marlene Gilles. Breast Conservative Surgery pilot study: data acquisition design and image processing. Master’s thesis, Department of Computer Science, University of Houston, July 2012.
- [14] M. Hansard, S. Lee, O. Choi, and R.P. Horaud. *Time-of-Flight Cameras Principles, Methods and Applications*. Springer, November 2012.
- [15] R. Hartley and A. Zisserman. *Multiple View Geometry in Computer Vision*. Cambridge University Press, March 2004.
- [16] Yi Liu, Dongming Zhang, Junbo Guo, and Shouxun Lin. Stripe Model: An Efficient Method to Detect Multi-form Stripe Structures. *Advances in Multimedia Modeling*, 7732:425–435, 2013.
- [17] Microsoft. Xbox 360 + kinect. <http://www.xbox.com/en-US/kinect?xr=shellnav>.
- [18] National Cancer Institute. Breast Cancer. <http://www.cancer.gov/dictionary?CdrID=444971>.
- [19] Richard A. Newcombe, Shahram Izadi, Otmar Hilliges, and et al. KinectFusion: Real-Time Dense Surface Mapping and Tracking. *IEEE ISMAR*, October 2011.
- [20] Simon Placht, Joseph Stancanella, Christian Schaller, Michael Balda, and Elli Angelopoulou. Fast time-of-flight camera based surface registration for radiotherapy patient positioning. *Medical Physics*, 39:4–17, January 2012.
- [21] Fabio Remondino and David Stoppa. *TOF Range-Imaging Cameras*. Springer Berlin Heidelberg, January 2013.
- [22] J. Salvi, X. Armangué, and J. Batlle. A comparative review of camera calibrating methods with accuracy evaluation. *Pattern Recognition*, 35:1617–1635, 2002.

- [23] Christian Schaller, Jochen Penne, and Joachim Hornegger. Time-of-flight sensor for respiratory motion gating. *Visualization and Computer Graphics, IEEE Transactions*, 12, April 2008.
- [24] D. Scharstein and R. Szeliski. High-accuracy stereo depth maps using structured light. *Computer Vision and Pattern Recognition, 2003. Proceedings. 2003 IEEE Computer Society Conference on*, 1:I-195 – I-202, June 2003.
- [25] D. Thanoon. *Computational Framework for Breast Cancer*. PhD thesis, Department of Computer Science, University of Houston, December 2011.
- [26] D. Thanoon, M. Garbey, and B.L Bass. Computational Modeling of Breast Conserving Surgery (BCS) starting from MRI Imaging. *JSSCM*, 5, November 2011.
- [27] Jing Tong, Jin Zhou, Ligang Liu, Zhigeng Pan, and Hao Yan. Scanning 3D Full Human Bodies using Kinects. *Visualization and Computer Graphics, IEEE Transactions*, 18, April 2012.
- [28] Emanuele Trucco and Alessandro Verri. *Introductory Techniques for 3-D Computer Vision*. Prentice Hall, 1998.
- [29] Luminita A. Vese and Tony F. Chan. A Multiphase Level Set Framework for Image Segmentation Using the Mumford and Shah Model. *International Journal of Computer Vision*, 50:271–293, December 2002.
- [30] Thomas P. Weldon and William E. Higgins. Design Of Multiple Gabor Filters For Texture Segmentation. *ICASSP*, 4:2243–2246, 1996.
- [31] Yonatan Wexler, Andrew W. Fitzgibbon, and Andrew Zisserman. Learning epipolar geometry from image sequences. *Proceedings of the IEEE Conference on Computer Vision and Pattern Recognition*, 2:209–216, January 2003.
- [32] World Health Organization. Cancer. <http://www.who.int/mediacentre/factsheets/fs297/en/index.html>.
- [33] Chang Ying, Ren Hong-e, and Dong Ben-zhi. An improved algorithm for feature point matching. *Environmental Science and Information Application Technology (ESIAT)*, 4:112–115, 2010.
- [34] ZooFari. Epipolar geometry. http://en.wikipedia.org/wiki/Epipolar_geometry.